Multifunctional probe based on modified Ag&Mn:ZnInS QDs for dual-mode fluorescence and magnetic resonance imaging of intracellular glutathione

Yibing Liu [a], Xue Jiang [b], Wei Wang [a], Wei Zhang [a], Xinghua Wang [a], Ying Sun [a], Yibing Huang [b], Pinyi Ma [a,*], Daqian Song [a,**]

[a] College of Chemistry, Jilin Province Research Center for Engineering and Technology of Spectral Analytical Instruments, Jilin University, Qianjin Street 2699, Changchun, 130012, China
[b] Key Laboratory for Molecular Enzymology and Engineering of the Ministry of Education, School of Life Sciences, Jilin University, Qianjin Street 2699, Changchun, 130012, China

HIGHLIGHTS

- We developed a GSH-responsive Ag&Mn:ZnInS QDs@SiO₂–MnO₂-HA probe for dual-mode fluorescence and magnetic resonance imaging.
- In the presence of GSH, MnO_2 was reduced to Mn^{2+}, causing the dual-modal property of the probe to turn on.
- The near-infrared emission probe was successfully employed in imaging of GSH in living cells and zebrafish due to its low toxicity and high anti-biological interference performance.

GRAPHICAL ABSTRACT
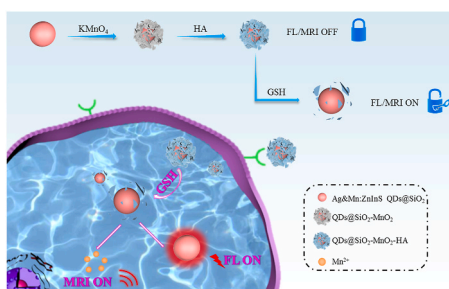
ARTICLE INFO

ABSTRACT

Glutathione (GSH) plays vital roles in a variety of biological processes, and the development of simple and effective GSH detection method is an important research topic. Herein, a multifunctional probe based on Ag&Mn: ZnInS quantum dots (QDs) was developed for bimodal imaging of GSH. MnO_2, as an efficient fluorescence quencher, was in-situ grown on the surface of QDs, and then modified with hyaluronic acid (HA) to improve the stability and targeted recognition capability of the probe due to the binding between HA and CD44 receptors. After MnO_2 was deconstructed by GSH, the fluorescence of the probe was recovered and the generated Mn^{2+} could serve as good magnetic resonance imaging (MRI) contrast agent. Moreover, the near-infrared emission probe was successfully employed in living cell and zebrafish imaging due to its low toxicity and high anti-biological interference performance. This strategy provides a simple dual-mode fluorescence/MRI imaging of GSH, which may have a broad application in biological detection.

1. Introduction

Glutathione (GSH), which is composed of glutamic acid, cysteine, and glycine, is the most common intracellular biothiol in living organisms [1–3]. GSH plays an important role in various physiological functions such as maintaining redox homeostasis, detoxification and resistance to free radicals [4–6]. Abnormal levels of GSH are related to a variety of diseases, including cancer, cardiovascular disease, neurodegenerative disease and so on [7–9]. Tumor cells are rich in GSH; therefore, accurate measurement and imaging of intracellular GSH could significantly assist in early diagnosis of tumors [10,11]. Various analytical techniques have been developed to detect the GSH levels in efforts to better understand its pathological and physiological functions.

Compared to that of previously reported methods, the use of fluorescence technology in biological detection has attracted great attention, due to its advantages of simplicity, cost-effectiveness, real-time monitoring capability and feasibility in cellular imaging [12,13]. However, fluorescence imaging has some disadvantages, such as poor tissue permeability and obvious limitations in terms of depth [14]. Magnetic resonance imaging (MRI) with high spatial resolution and tissue penetration is an attractive technique for *in vivo* studies and clinical diagnosis [15,16]. This method can effectively improve the detection accuracy and expand the scope of practical application [17]. Nowadays, a great deal of research has been devoted to the construction of MRI probes, such as lanthanide-doped Y_2O_3 nanoprobes [18] and superparamagnetic iron oxide nanoparticles [19]. MnO_2 is widely used as an MRI agent, because Mn^{2+} produced from its decomposition is a type of paramagnetic relaxation signaling agent [20–22]. Therefore, the development of intelligent bimodal imaging nanoprobes based on fluorescence and MRI for early diagnosis of various diseases can be greatly valuable.

Semiconductor quantum dots (QDs) exhibits unique optical properties, such as size-dependent photoluminescence, high quantum yields and large Stokes shift; thus, they can serve as effective tools for biosensing and bio-labeling [23–26]. Among the many types of QDs, near-infrared QDs have attracted widespread attention due to their better penetration ability and anti-biological interference performance [27–29]. In order to better use QDs in biological application, it is necessary to develop near-infrared emitting QDs without highly toxic elements. Ag/Mn co-doped ZnInS QDs with excellent photoluminescence performance and low toxicity have great potential in bioimaging applications [30–32]. However, research on these QDs has seldom been reported, and it is of great significance to investigate the application of these materials.

Herein, a multifunctional probe for GSH detection, living cell imaging, MRI imaging and differentiation between cancer cells and normal cells was developed. The probe had dual-mode imaging capability and could induce different signal responses by using a single trigger, which brought simplicity to the analysis process while improved its accuracy. MnO_2 was in-situ grown on Ag&Mn:ZnInS QDs@SiO$_2$, the surface of which was then coated with hyaluronic acid (HA) to improve the stability and targeted recognition capability, due to the specific binding between HA and CD44 receptors which are usually overexpressed on the surface of cancer cells [33]. In the presence of GSH, MnO_2 was decomposed into Mn^{2+} causing the fluorescence intensity of QDs to be restored and the generated Mn^{2+} could also serve as a good MRI contrast agent. In addition, the probe had near-infrared emission, thus possessed excellent anti-biological interference performance. It was also successfully applied to image living cells, lysosome localization, discrimination between cancer cells and normal cells, and living zebrafish imaging, which demonstrated that the probe had excellent biocompatibility and can be applied in various diagnoses.

2. Experimental section

2.1. Synthesis of Ag&Mn:ZnInS QDs and QDs@SiO$_2$

Hydrophobic Ag&Mn:ZnInS QDs were synthesized based on our previous work [32]. For aqueous phase transfer by silanization, a two-step process was carried out [34]. Firstly, 2 µL of TEOS was added to 1 mL of toluene solution of Ag&Mn:ZnInS QDs (10 mg mL^{-1}), and the mixture was then stirred for 5 h to obtain precursor solution A. Secondly, 2 µL of MPS in 6 mL of ethanol, 0.5 mL of H$_2$O and 0.1 mL of ammonia (25 wt%) were stirred for more than 12 h to obtain precursor solution B. Finally, the precursor solutions A and B were mixed and then stirred for 4 h, and the mixture was then centrifuged at 15,000 rpm for 30 min; and the precipitate was then re-dispersed in water for further use.

2.2. Synthesis of QDs@SiO$_2$–MnO$_2$ and QDs@SiO$_2$–MnO$_2$-HA

For MnO_2 coating, 200 µL of the prepared QDs@SiO$_2$ (1.5 mg mL^{-1}) was mixed with 250 µL of KMnO$_4$ solution (1.2 mM) and 1 mL of H$_2$O and then treated with ultrasound for 40 min. To obtain QDs@SiO$_2$–MnO$_2$, the mixture was centrifuged at 15,000 rpm for 15 min, and the precipitate was collected and re-dispersed in 1 mL of water. For the synthesis of QDs@SiO$_2$–MnO$_2$-HA, 1 mL of QDs@SiO$_2$–MnO$_2$ was mixed with 1 mg of HA and then stirred for 12 h. The precipitates were collected by centrifugation at 15,000 rpm for 15 min and then re-dispersed in 1 mL of water.

2.3. Fluorometric detection of GSH

For GSH detection, 50 µL of QDs@SiO$_2$–MnO$_2$-HA (0.25 mg mL^{-1}) was mixed with 100 µL of GSH solution at different concentrations and 850 µL of PBS solution (10 mM, pH 5.5). After incubating for 5 min at room temperature, the fluorescence spectra of the mixture were measured at an excitation wavelength of 350 nm.

2.4. MTT assay and cell imaging

For MTT assay, HepG2 cells were cultured in a 96-well plate and were thereafter treated with different concentrations of QDs@SiO$_2$ (0.005–0.15 mg mL^{-1}) and QDs@SiO$_2$–MnO$_2$-HA (0.1–0.5 mg mL^{-1}) for 24 h at 37 °C. After 5 mg mL^{-1} MTT solution was added into each well, the cells were further incubated for 4 h. After the addition of 150 µL of dimethyl sulfoxide (DMSO), an absorbance at 490 nm of the cells was recorded using a microplate reader.

For intracellular GSH imaging, HepG2 cells were incubated with QDs@SiO$_2$–MnO$_2$-HA (0.5 mg mL^{-1}) for 30 min or 1 h. To decrease the GSH concentration in living cells, HepG2 cells were treated with NEM (500 µM) for 20 min before incubating with QDs@SiO$_2$–MnO$_2$-HA for 1 h. LO2 cells (normal cells) were incubated with QDs@SiO$_2$–MnO$_2$-HA (0.5 mg mL^{-1}) for 1 h. For lysosomes co-localization, the cells were treated with QDs@SiO$_2$–MnO$_2$-HA (0.5 mg mL^{-1}) for 30 min, followed by LysoTracker Green (a lysosome-specific fluorescent dye) for another 30 min. The confocal fluorescent images were carried out on an LSM 710 (CarlZeiss) confocal microscope after the cells were washed three times with PBS.

2.5. Magnetic resonance imaging of the probe

The T$_1$-and T$_2$-weighted images were acquired on a Siemens Prisma 3.0 T MR scanner (Erlangen, Germany) with a gradient strength of up to 80 mT/m. The images of different concentrations of QDs@SiO$_2$–MnO$_2$-HA with and without 5 mM GSH were measured. The concentrations of Mn were determined by ICP-OES. The T$_1$-weighted scanning parameters were set as: TR=6000 ms, TE=20 ms, IR=30, 60, 90, 200, 500, 1000 ms; The T$_2$-weighted scanning parameters were set as: TR=6000 ms, TE=15, 20, 25, 30, 35, 50, 70, 100 ms.
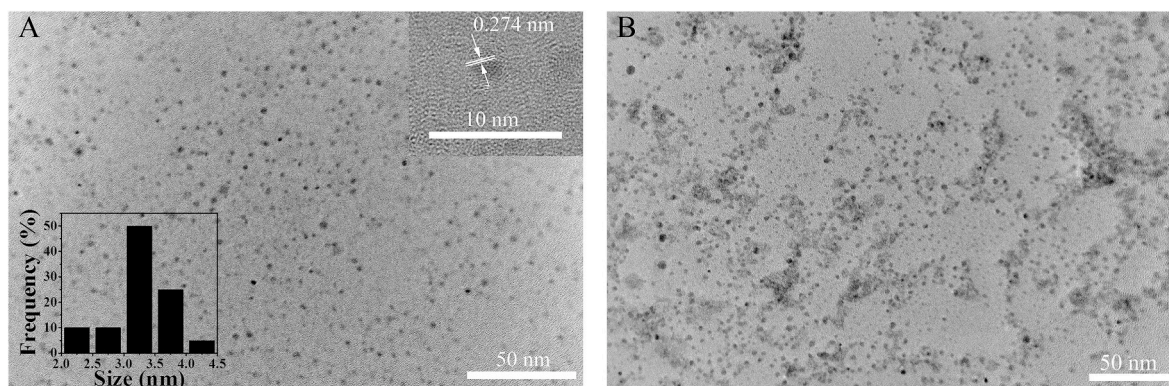
Fig. 1. (A) TEM image and size distribution histogram (inset) of Ag&Mn:ZnInS QDs@SiO$_2$. (B) TEM image of QDs@SiO$_2$–MnO$_2$-HA.

3. Results and discussion

3.1. Characterization and sensing mechanism

The TEM image (Fig. 1A) showed that Ag&Mn:ZnInS QDs@SiO$_2$ was uniformly dispersed spherical particles with an average size of 3.25 nm. The lattice spacing was 0.274 nm, which could be attributed to the (102) planes of zinc-blend ZnInS QDs [35]. As displayed in Fig. S1, the optimal excitation and emission wavelengths of QDs were 350 nm and 660 nm, respectively. The quantum yield of QDs was determined by the relative comparison procedure, using freshly prepared analytical purity quinine sulfate in 0.1 M H$_2$SO$_4$ as a relative quantum yield standard. The relative quantum yield was calculated to be about 0.05. Fig. S2 showed the TEM image and size distribution histogram of hydrophobic Ag&Mn:ZnInS QDs. QDs@SiO$_2$–MnO$_2$-HA was synthesized by a one-pot reaction of in-situ grow MnO$_2$ on the surface of QDs. The TEM image in Fig. 1B and Fig. S3 showed that QDs@SiO$_2$ was coated with MnO$_2$ and no obvious morphological or structural changes were visually observed. Fig. S4 was the photograph of QDs@SiO$_2$, QDs@SiO$_2$–MnO$_2$ and QDs@SiO$_2$–MnO$_2$-HA before and after being placed for 3 days. As can be seen, without

the modification with HA, the system was unstable and prone to coagulation. However, QDs@SiO$_2$–MnO$_2$-HA remained stable and well-dispersed even after being let stand for 3 days. In addition to improving stability, HA is a natural polysaccharide that can also improve biocompatibility and tumor-targeting ability of the probe by specifically binding to CD44 receptors [36]. The Zeta potential of QDs@SiO$_2$–MnO$_2$ changed from −14.4 to −23.2 mV after the HA modification, which confirming the successful decoration of HA (Fig. S5A). Moreover, the dynamic light scattering (DLS) data (Figs. S5B and S5C) showed the mean size of QDs@SiO$_2$–MnO$_2$ and QDs@SiO$_2$–MnO$_2$-HA was 243.6 nm and 263.2 nm, respectively. As shown in the FT-IR spectra (Fig. S6), the peaks around 1609 cm^{-1} (amide I), 1560 cm^{-1} (amide II) and 1376 cm^{-1} (amide III) were owing to the presence of amide bond in HA. The peaks at 2885 cm^{-1} and 3430 cm^{-1} were attributed to the C–H stretching and –OH stretching vibrations of HA [36].

The elemental composition of QDs@SiO$_2$ (Fig. S7) and QDs@SiO$_2$–MnO$_2$-HA (Fig. S8) was examined by energy-dispersive spectrometry (EDS). After MnO$_2$ coating, the percentage of Mn increased compared with that before modification. The UV–vis
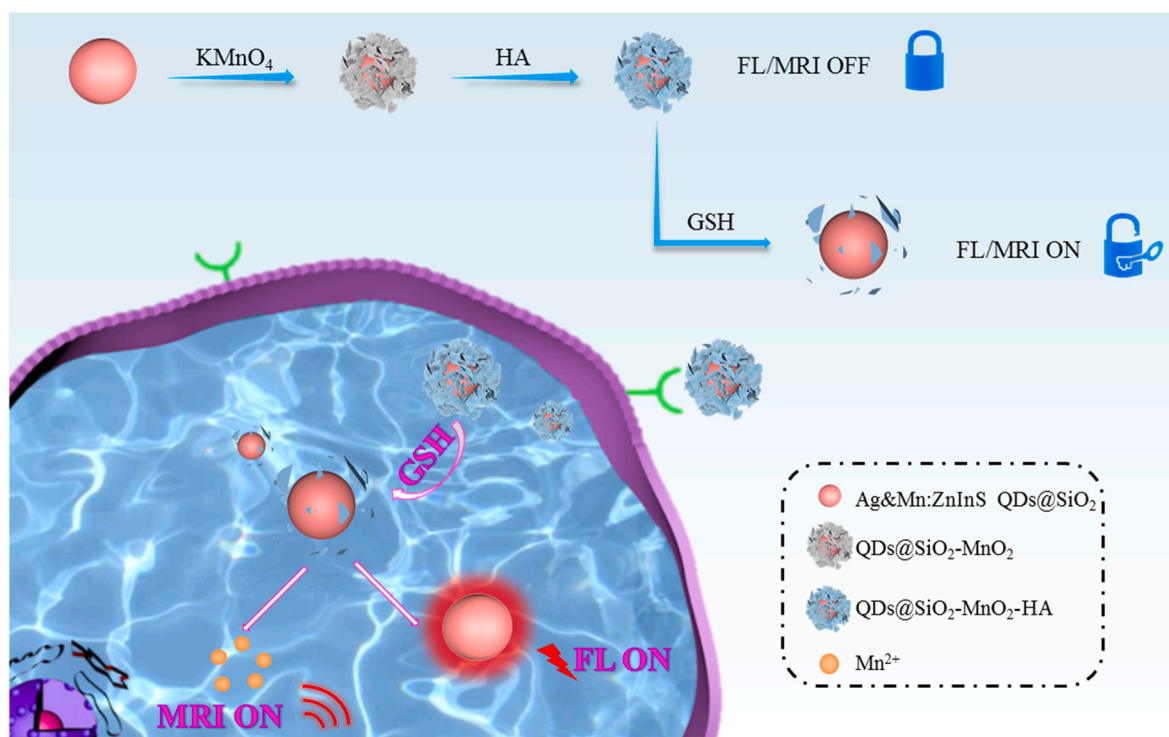
Scheme 1. Schematic diagram of GSH-responsive probe in fluorescence/MRI dual-mode imaging.
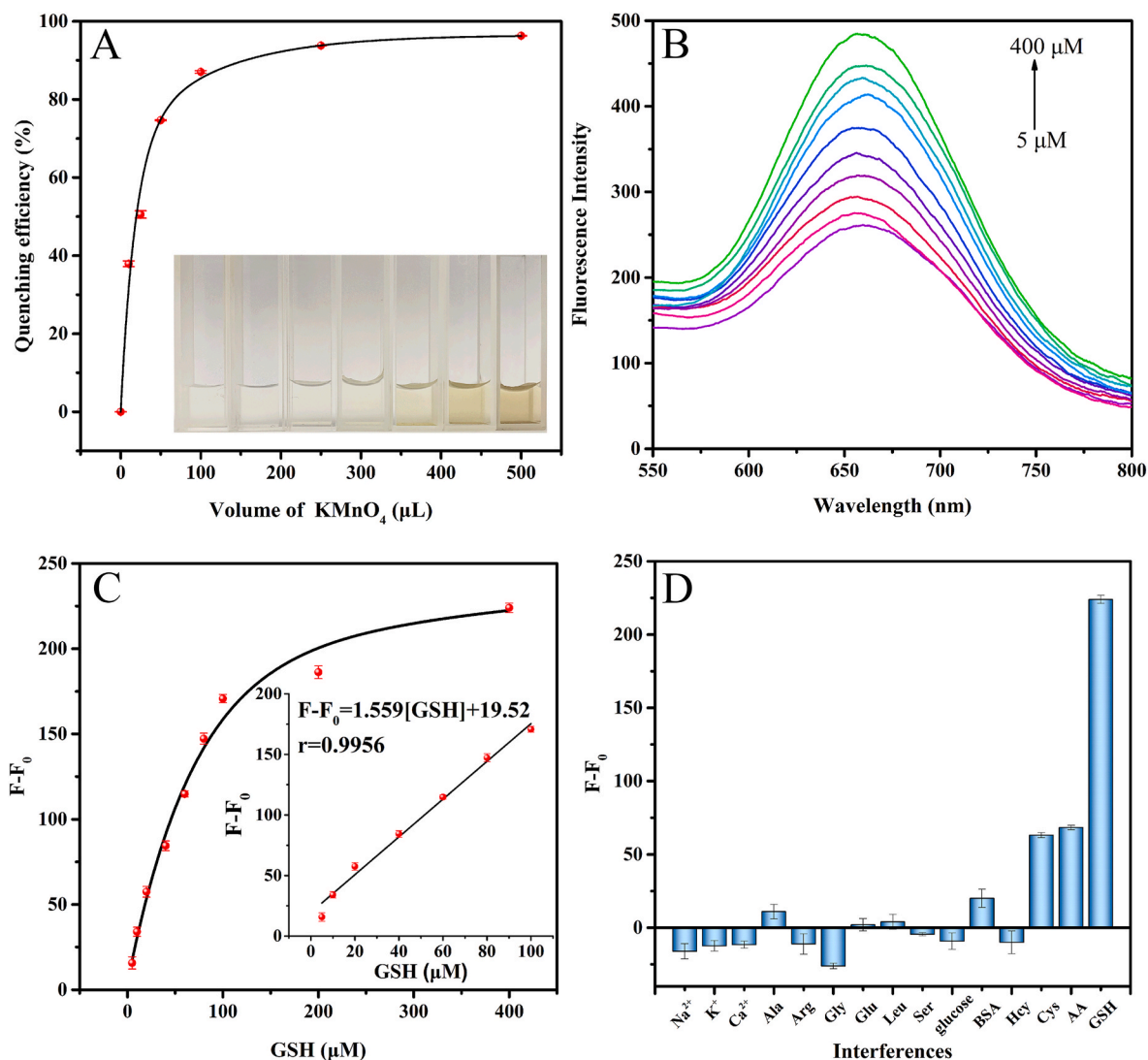
Fig. 2. (A) Dependency of fluorescent quenching efficiency on $KMnO_4$ (1.2 mM) volume. The inset shows the corresponding color changes of $QDs@SiO_2–MnO_2$ solution upon the addition of $KMnO_4$. (B) Fluorescence spectra of $QDs@SiO_2–MnO_2$-HA with different concentrations of GSH. (C) Linear relationship between $F–F_0$ and GSH concentration (F_0/F: the fluorescence intensity before/after the addition of GSH). (D) Fluorescence intensity change of the probe in the presence of different interfering substances (100 μM for GSH, AA and Cys, 500 μM for other interferences). (For interpretation of the references to color in this figure legend, the reader is referred to the Web version of this article.)

absorption spectrum displayed in Fig. S9 indicated that $QDs@SiO_2$ exhibited no obvious absorption peak. However, after MnO_2 was in-situ grown, an absorption peak located at 375 nm appeared due to the generation of MnO_2 [29]. After modifying $QDs@SiO_2–MnO_2$ with HA, no obvious change of absorption peak was observed. To study the quenching effect of MnO_2 on QDs, time–resolved fluorescence decay of $QDs@SiO_2$ and $QDs@SiO_2–MnO_2$-HA was measured. As shown in Fig. S10, the fluorescence lifetime decreased dramatically, indicating a potential fluorescence resonance energy transfer (FRET) between QDs and MnO_2.

MnO_2, as an efficient fluorescence quencher, can quench the fluorescence of QDs and produce Mn^{2+}, which can be used as an MRI agent, after being decomposed by GSH. As illustrated in Scheme 1, after in-situ generation of MnO_2 and HA modification on the surface of QDs, the fluorescence and MRI property were inhibited. GSH exhibited strong reducing ability, which can reduce MnO_2 to Mn^{2+} and inhibit the FRET process between QDs and MnO_2. Thus, the fluorescence could be recovered and the dual-modal property of the probe was turned on. The above showed that a GSH-responsive dual-modal imaging probe based on $QDs@SiO_2–MnO_2$-HA was successfully developed.

3.2. Fluorescence response of the probe to GSH

To ensure the best performance of the probe, several factors affecting the detection process were optimized, such as the content of $KMnO_4$, pH value and reaction time. As depicted in Fig. 2A, the degree of quenching was dependent on the content of $KMnO_4$, and it reached a plateau when the volume of 1.2 mM $KMnO_4$ was 250 μL. The fluorescence intensity of $QDs@SiO_2–MnO_2$-HA with and without GSH at different pH values was investigated. As displayed in Fig. S11, acidic conditions could better facilitate the MnO_2 decomposition compared with the neutral and alkaline conditions, and the probe remained stable without GSH under different pH. Therefore, pH 5.5, which is also the pH of the weak acidic environment of tumors and cancer cells, was chosen as the optimal pH value. As displayed in Fig. S12, the fluorescence recovery after the addition of GSH reached a plateau in 5 min.

Under the optimal conditions, the applicability of the proposed probe in GSH detection was investigated. Fig. 2B showed the change of fluorescence intensity in the presence of varying concentrations of GSH. At a concentration range of 5–400 μM, the fluorescence of the probe was gradually recovered as the GSH concentration increased. A good linear
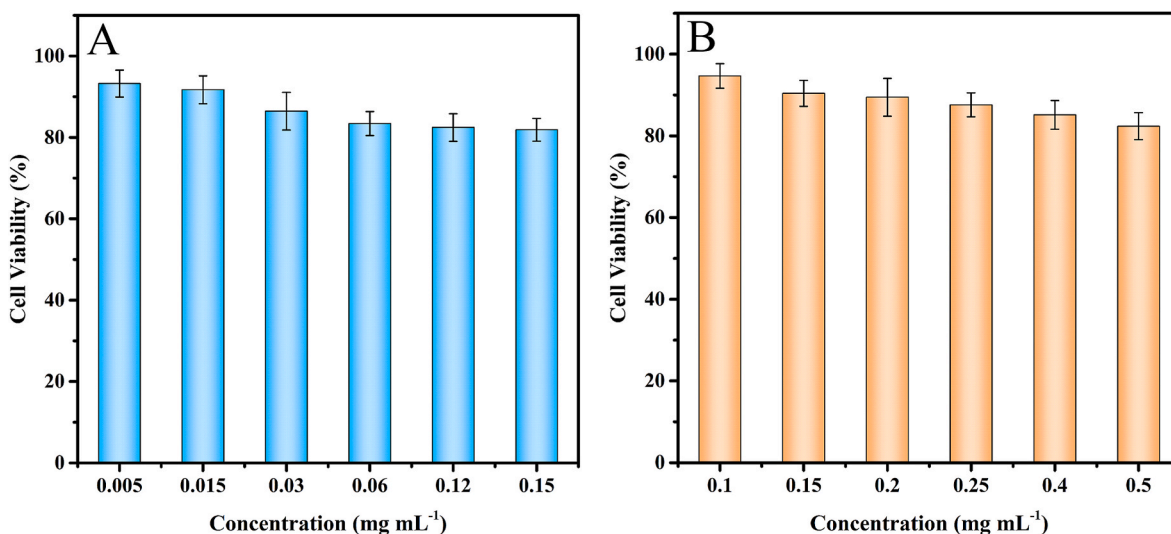
Fig. 3. Viability of HepG2 cells (model cells) incubated with (A) Ag&Mn:ZnInS QDs@SiO$_2$ and (B) QDs@SiO$_2$–MnO$_2$-HA.

relationship between F–F$_0$ and GSH concentration was obtained at the GSH concentration ranging from 5 to 100 μM with a linear regression equation of F–F$_0$ = 1.559[GSH] + 19.52 and an r value of 0.9956 (Fig. 2C). The limit of detection (LOD) calculated based on 3σ/k rule was 2.78 μM. The sensing performance comparison of this method with other methods was listed in Table S1. Although the LOD of our probe was not the lowest among all probes listed, it was much lower than the concentrations of GSH in human serum and living cells (0.5–10 mM) [37]; thus, our probe should be sufficient for routine detection. In living cell imaging, a probe with too low LOD may be susceptible to interference by ascorbic acid and cysteine (μM level). In addition, our probe was located in the near-infrared fluorescent region, and the quantum yield of QDs was not as good as that in the ultraviolet–visible region, which could also affect the sensitivity of the near-infrared probe [29]. However, the near-infrared probe has superior anti-biological interference performance and is more suitable for cell imaging.
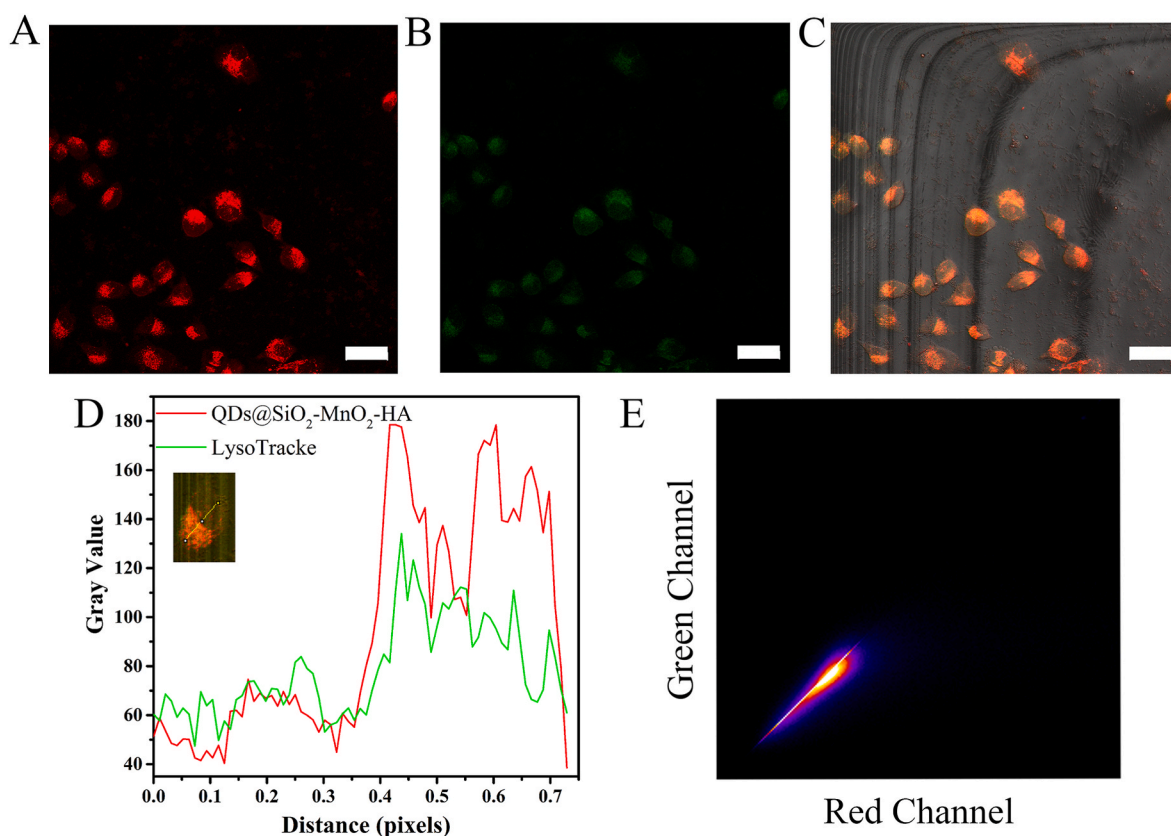

Fig. 4. Confocal fluorescence images of HepG2 cells incubated with (A) 0.5 mg mL^{-1} QDs@SiO$_2$–MnO$_2$-HA (red channel) and (B) LysoTracker Green (green channel). (C) Merged image wherein yellow represents the superimposition of the red and green fluorescence. (D) Intensity profiles of QDs@SiO$_2$–MnO$_2$-HA and LysoTracker. (E) A plot showing intensity correlation between QDs@SiO$_2$–MnO$_2$-HA and LysoTracker. Scale bar: 50 μm. (For interpretation of the references to color in this figure legend, the reader is referred to the Web version of this article.)
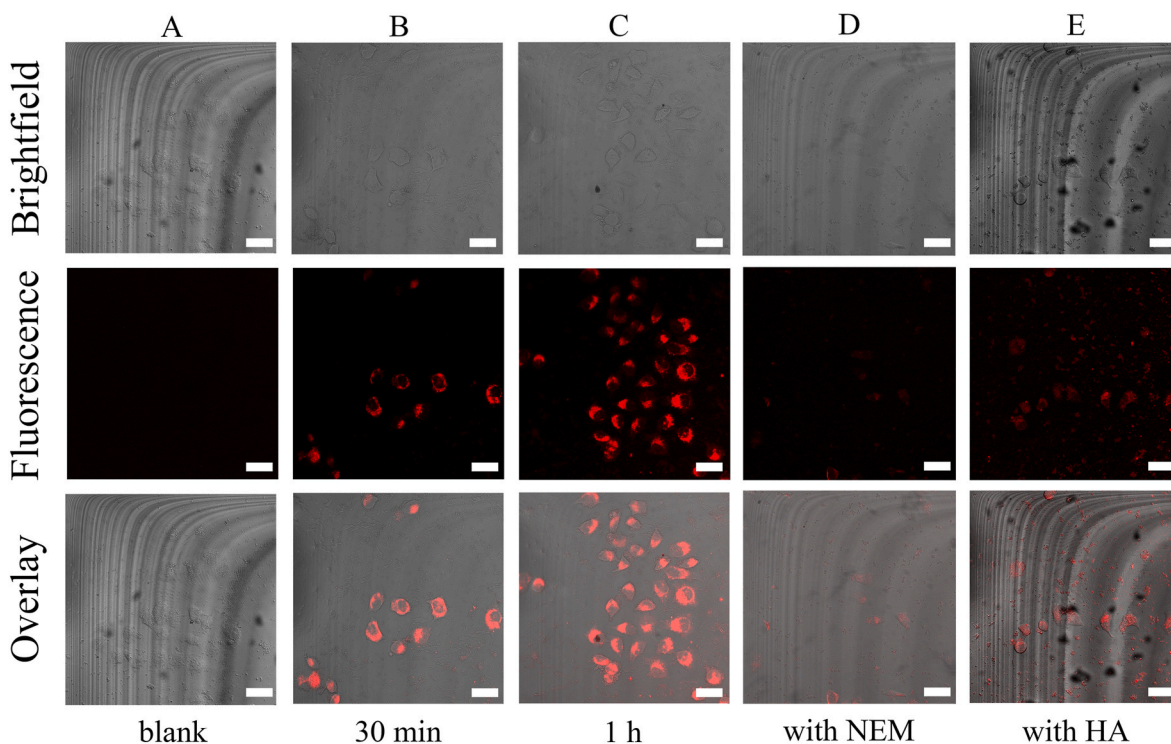
Fig. 5. Confocal fluorescence images of HepG2 cells: (A) cells only; (B) cells incubated with QDs@SiO$_2$–MnO$_2$-HA (0.5 mg mL^{-1}) for 30 min; (C) cells incubated with QDs@SiO$_2$–MnO$_2$-HA (0.5 mg mL^{-1}) for 1 h; (D) cells pretreated with NEM (500 μM) for 20 min, followed by incubation with QDs@SiO$_2$–MnO$_2$-HA (0.5 mg mL^{-1}) for 1 h. (E) cells pretreated with HA (5 mg mL^{-1}) for 1 h, followed by incubation with QDs@SiO$_2$–MnO$_2$-HA (0.5 mg mL^{-1}) for 1 h. Scale bar: 50 μm.
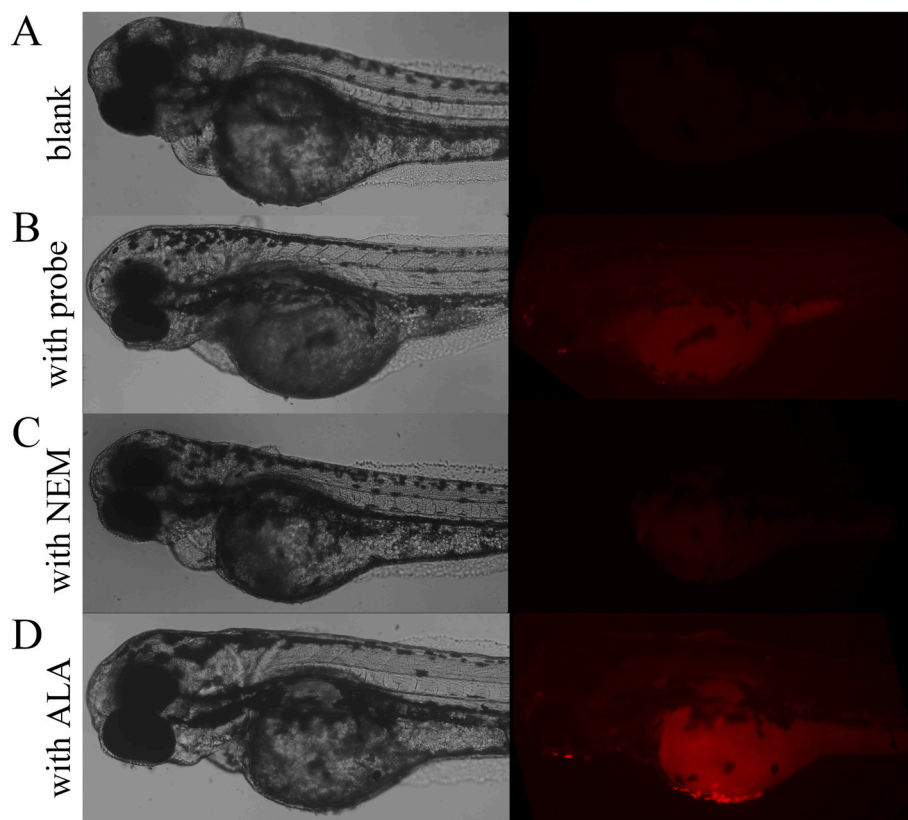

Fig. 6. Fluorescence images of zebrafish: (A) zebrafish only; (B) zebrafish incubated with QDs@SiO$_2$–MnO$_2$-HA (0.5 mg mL^{-1}) for 1 h; (C) zebrafish pretreated with NEM (500 μM) for 20 min, followed by incubation with QDs@SiO$_2$–MnO$_2$-HA (0.5 mg mL^{-1}) for 1 h. (E) zebrafish pretreated with ALA (500 μM) for 2 h, followed by incubation with QDs@SiO$_2$–MnO$_2$-HA (0.5 mg mL^{-1}) for 1 h.
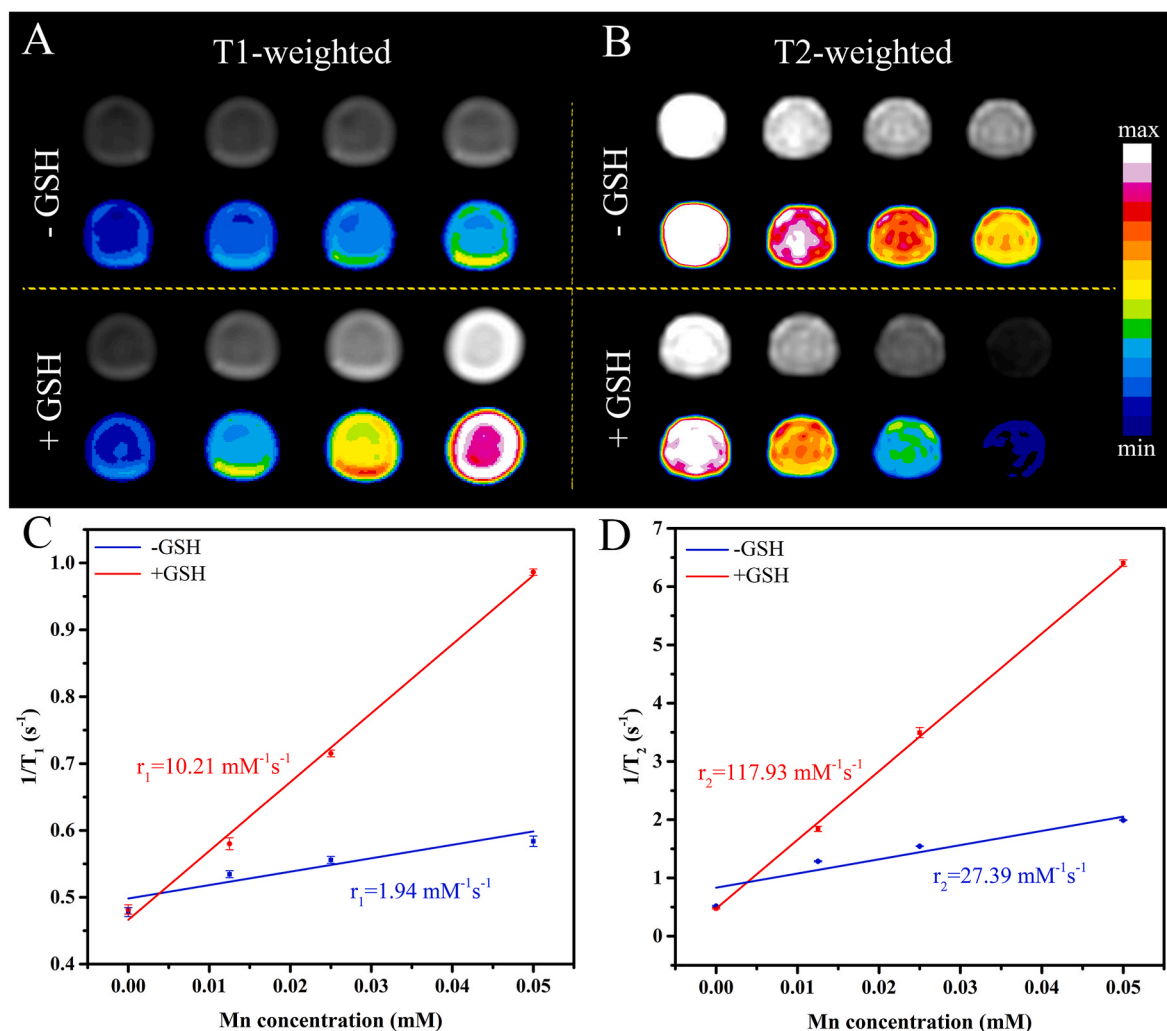
Fig. 7. (A) T_1-weighted and (B) T_2-weighted MRI images of QDs@SiO$_2$–MnO$_2$-HA at different concentrations in the presence and absence of 5 mM GSH. (C) Plots of $1/T_1$ and (D) $1/T_2$ versus Mn concentration in the presence and absence of GSH.

3.3. Effects of interferences and analysis of human serum sample

To prove the capability of the established probe in specific detection of GSH, the fluorescence intensity change upon the addition of potential interference substances was investigated. The influence of 500 μM each of Na$^+$, K$^+$, Ca^{2+}, amino acids including alanine (Ala), arginine (Arg), glycine (Gly), glutamic acid (Glu), leucine (Leu), and serine (Ser), glucose, bovine serum albumin (BSA) and homocysteine (Hcy), as well as 100 μM each of cysteine (Cys) and ascorbic acid (AA) without and with 100 μM GSH, were assessed. As shown in Fig. 2D and Fig. S13, the fluorescence change caused by 100 μM GSH was significantly higher than that caused by other interfering substances at relatively high concentrations. Although Cys and AA at the same concentration as that of GSH could cause slight fluorescence recovery, their concentration in the biological systems was much lower than that of GSH [38]. Thus, their influence on GSH detection was negligible, demonstrating the excellent selectivity of the proposed method.

Determination of GSH in human serum samples was conducted to evaluate the practicality and feasibility of the probe. Standard addition method was used to determine the GSH concentrations. As shown in Table S2, the average recoveries were in the range of 95.45–105.3% with relative standard deviations (RSD) between 1.8% and 2.8%. These results indicated that the probe could reliably apply to detect real samples.

3.4. Living cell imaging and zebrafish imaging

To evaluate the feasibility of the probe to apply in intracellular fluorescence imaging, MTT assay was employed to determine its cytotoxicity. As indicated in Fig. 3, the viability of HepG2 cells was higher than 80% when the concentration of QDs@SiO$_2$ was 0.15 mg mL^{-1} and the concentration of QDs@SiO$_2$–MnO$_2$-HA reached 0.5 mg mL^{-1}. These results demonstrated that the probe had low cytotoxicity and good biocompatibility, thus was suitable for living cell imaging.

The subcellular distribution of QDs@SiO$_2$–MnO$_2$-HA was evaluated by co-localization experiments. As can be seen in Fig. 4, red fluorescence of the probe can be clearly observed in the cell cytoplasm and lysosome, which was due to the endocytic delivery route of the probe in cells. Green fluorescence represented the labeling of lysosomes by using LysoTracker Green (a lysosome-specific fluorescent dye). As can be seen, the red fluorescence of the probe well-overlapped with the green fluorescence of LysoTracker Green to yellow. According to the intensity correlation diagram (Fig. 4D and E), the Pearson's correlation coefficient was calculated to be 0.98, which demonstrated the lysosome-targeting ability of the probe.

The fluorescence imaging of intracellular GSH was carried out using HepG2 cells. As displayed in Fig. 5, the increase of fluorescence intensity of cells incubated with the probe for 1 h was higher than that incubated for 30 min. The high concentration of GSH in cancer cells could decompose MnO$_2$, resulting in the recovery of quenched fluorescence.

After treating with NEM (thiol-reactive inhibitors) before adding the probe, significant reduction of fluorescence was observed. These results indicated that the probe can be employed in the imaging of intracellular GSH. To study the HA receptor-mediated endocytosis, HepG2 cells were pretreated with free HA. The red fluorescence was lower, which was due to the fact that HA specifically bound to the CD44 receptor and inhibited the cellular HA receptor-mediated pathway. The difference between the GSH concentration inside cancer cells and that in normal cells can be used as a marker to distinguish between them. Cancer cells have a higher level of GSH, which contributes to their highly reduced environment [39]. Therefore, the confocal imaging of LO2 cells (normal cells) incubated with the probe was investigated (Fig. S14). Due to the low concentration of GSH in normal cells, the fluorescence signal was very weak. Herein, we speculate that the probe can be used to differentiate between normal and cancer cells, as the latter can restore the fluorescence signal.

We further investigated the applicability of the probe for *in vivo* imaging, as displayed in Fig. 6, endogenous GSH imaging in living zebrafish was studied. As expected, nearly no fluorescence was observed in blank zebrafish. In the presence of the probe, apparent red fluorescence signal was found after 1 h incubated at 26 °C. Moreover, when the zebrafish was incubated with 500 μM NEM in the presence of the probe, dramatically reduced fluorescence was observed. And the fluorescence signal was enhanced when the zebrafish was incubated with 500 μM ALA (alpha lipoic acid, GSH enhancer). These results demonstrated that the probe could be used to monitor the expression level of GSH in living zebrafish.

3.5. MRI property of the probe

Mn^{2+} generated as a result of MnO_2 decomposition can serve as an activatable MRI contrast agent; thus, the effectiveness of the probe as a GSH-activated MRI contrast agent was studied. QDs@SiO$_2$–MnO$_2$-HA at different concentrations was incubated with 5 mM GSH, and the samples were subjected to T_1-weighted and T_2-weighted MRI imaging. As shown in Fig. 7A, in the absence of GSH, the T_1-weighted MRI signal was weak. After reacting with GSH, a significant enhancement of the MRI signal was observed, and the signal increased with the increase of Mn concentration. Similar results were observed in T_2-weighted MRI images; however, the T_2-weighted MRI signal decreased with the increase of Mn concentration (Fig. 7B). The T_1 and T_2 values were measured, and the relationships between $1/T_1$ and $1/T_2$ with Mn concentration were plotted (Fig. 7C and D). The longitudinal relaxivity r_1 was calculated to be 10.21 mM^{-1} s^{-1}, while the transverse relaxivity r_2 was calculated to be 117.93 mM^{-1} s^{-1}. Compared with the probe in the absence of GSH, r_1 was enhanced by 5.26–fold, whereas r_2 was enhanced by 4.31–fold, demonstrating that the probe had excellent GSH-responsive MRI performance.

4. Conclusion

To sum up, we successfully constructed a GSH-responsive Ag&Mn: ZnInS QDs@SiO$_2$–MnO$_2$-HA probe for dual-mode fluorescence and magnetic resonance imaging. Fluorescence and MRI signals could be turned off by the in-situ generated MnO$_2$. In the presence of GSH, MnO$_2$ could be reduced to Mn^{2+}, causing the dual-modal property of the probe to turn on. Due to its good biocompatibility and resistance to external interferences with near-infrared emission, the probe was successfully employed in the imaging of living cells and zebrafish, lysosome localization, and in the discrimination of cancer cells from normal cells. With its satisfactory results, the probe has a potential in biological detection. The probe was conveniently designed and effective for GSH detection and imaging, thus can be applied to research on cancer cell imaging and clinical diagnosis.

References

[1] H.J. Forman, H. Zhang, A. Rinna, Glutathione: overview of its protective roles, measurement, and biosynthesis, Mol. Aspect. Med. 30 (2009) 1–12.
[2] Y. Peng, C. Ye, R. Yan, Y. Lei, D. Ye, H. Hong, T. Cai, Activatable core-shell metallofullerene: an efficient nanoplatform for bimodal sensing of glutathione, ACS Appl. Mater. Interfaces 11 (2019) 46637–46644.
[3] S.C. Lu, Regulation of glutathione synthesis, Mol. Aspect. Med. 30 (2009) 42–59.
[4] M.H. Lee, Z. Yang, C.W. Lim, Y.H. Lee, S. Dongbang, C. Kang, J.S. Kim, Disulfide-cleavage-triggered chemosensors and their biological applications, Chem. Rev. 113 (2013) 5071–5109.
[5] H. Fan, G. Yan, Z. Zhao, X. Hu, W. Zhang, H. Liu, X. Fu, T. Fu, X.B. Zhang, W. Tan, A smart photosensitizer-manganese dioxide nanosystem for enhanced photodynamic therapy by reducing glutathione levels in cancer cells, Angew. Chem. 55 (2016) 5477–5482.
[6] Z.-Q. Hu, L.-L. Sun, Y.-Y. Gu, Y. Jiang, A sensitive and selective fluorescent probe for detection of glutathione in the presence of Cu2+ and its application to biological imaging, Sensor. Actuator. B Chem. 212 (2015) 220–224.
[7] D.M. Townsend, K.D. Tew, H. Tapiero, The importance of glutathione in human disease, Biomed. Pharmacother. 57 (2003) 145–155.
[8] W. Chen, X. Yue, H. Zhang, W. Li, L. Zhang, Q. Xiao, C. Huang, J. Sheng, X. Song, Simultaneous detection of glutathione and hydrogen polysulfides from different emission channels, Anal. Chem. 89 (2017) 12984–12991.
[9] K. Ngamchuea, C. Batchelor-McAuley, R.G. Compton, Rapid method for the quantification of reduced and oxidized glutathione in human plasma and saliva, Anal. Chem. 89 (2017) 2901–2908.
[10] H. Hu, J. Chen, H. Yang, X. Huang, H. Wu, Y. Wu, F. Li, Y. Yi, C. Xiao, Y. Li, Y. Tang, Z. Li, B. Zhang, X. Yang, Potentiating photodynamic therapy of ICG-loaded nanoparticles by depleting GSH with PEITC, Nanoscale 11 (2019) 6384–6393.
[11] F. Liang, S. Jiao, D. Jin, L. Dong, S. Lin, D. Song, P. Ma, A novel near-infrared fluorescent probe for the dynamic monitoring of the concentration of glutathione in living cells, Spectrochim. Acta, Part A 224 (2020) 117403.
[12] Y. Xu, Z. Zhang, P. Lv, Y. Duan, G. Li, B. Ye, Ratiometric fluorescence sensing of Fe2+/3+ by carbon dots doped lanthanide coordination polymers, J. Lumin. 205 (2019) 519–524.
[13] X.L. Zhang, C. Zheng, S.S. Guo, J. Li, H.H. Yang, G. Chen, Turn-on fluorescence sensor for intracellular imaging of glutathione using g-C(3)N(4) nanosheet-MnO(2) sandwich nanocomposite, Anal. Chem. 86 (2014) 3426–3434.
[14] P. Zhao, K. He, Y. Han, Z. Zhang, M. Yu, H. Wang, Y. Huang, Z. Nie, S. Yao, Near-infrared dual-emission quantum dots-gold nanoclusters nanohybrid via co-template synthesis for ratiometric fluorescent detection and bioimaging of ascorbic acid in vitro and in vivo, Anal. Chem. 87 (2015) 9998–10005.
[15] M.C. Cassidy, H.R. Chan, B.D. Ross, P.K. Bhattacharya, C.M. Marcus, In vivo magnetic resonance imaging of hyperpolarized silicon particles, Nat. Nanotechnol. 8 (2013) 363–368.
[16] R. Weissleder, M. Nahrendorf, M.J. Pittet, Imaging macrophages with nanoparticles, Nat. Mater. 13 (2014) 125–138.
[17] D.H. Ortgies, L. de la Cueva, B. Del Rosal, F. Sanz-Rodriguez, N. Fernandez, M. C. Iglesias-de la Cruz, G. Salas, D. Cabrera, F.J. Teran, D. Jaque, E. Martin Rodriguez, In vivo deep tissue fluorescence and magnetic imaging employing hybrid nanostructures, ACS Appl. Mater. Interfaces 8 (2016) 1406–1414.
[18] T.S. Atabaev, J.H. Lee, Y.C. Shin, D.W. Han, K.S. Choo, U.B. Jeon, J.Y. Hwang, J. A. Yeom, H.K. Kim, Y.H. Hwang, Eu, Gd-codoped yttria nanoprobes for optical and T(1)-weighted magnetic resonance imaging, Nanomaterials (2017) 7.
[19] Q. Chen, W. Shang, C. Zeng, K. Wang, X. Liang, C. Chi, X. Liang, J. Yang, C. Fang, J. Tian, Theranostic imaging of liver cancer using targeted optical/MRI dual-modal probes, Oncotarget 8 (2017) 32741–32751.
[20] Q. Wu, G. Chen, K. Gong, J. Wang, X. Ge, X. Liu, S. Guo, F. Wang, MnO2-Laden black phosphorus for MRI-guided synergistic PDT, PTT, and Chemother. Mat. 1 (2019) 496–512.
[21] X.T. Tian, P.P. Cao, H. Zhang, Y.H. Li, X.B. Yin, GSH-activated MRI-guided enhanced photodynamic- and chemo-combination therapy with a MnO2-coated porphyrin metal organic framework, Chem. Commun. 55 (2019) 6241–6244.

[22] Z. Zhao, H. Fan, G. Zhou, H. Bai, H. Liang, R. Wang, X. Zhang, W. Tan, Activatable fluorescence/MRI bimodal platform for tumor cell imaging via MnO2 nanosheet-aptamer nanoprobe, J. Am. Chem. Soc. 136 (2014) 11220–11223.

[23] L. Li, H. Lin, C. Lei, Z. Nie, Y. Huang, S. Yao, Label-free fluorescence assay for thrombin based on unmodified quantum dots, Biosens. Bioelectron. 54 (2014) 42–47.

[24] L. Liu, Q. Ma, Y. Li, Z. Liu, X. Su, A novel signal-off electrochemiluminescence biosensor for the determination of glucose based on double nanoparticles, Biosens. Bioelectron. 63 (2015) 519–524.

[25] Q. Xu, T. Kuang, Y. Liu, L. Cai, X. Peng, T. Sreenivasan Sreeprasad, P. Zhao, Z. Yu, N. Li, Heteroatom-doped carbon dots: synthesis, characterization, properties, photoluminescence mechanism and biological applications, J. Mater. Chem. B 4 (2016) 7204–7219.

[26] M. Y, K. Zhao, X. Zhu, S. Tang, Z. Nie, Y. Huang, P. Zhao, S. Yao, Development of near-infrared ratiometric fluorescent probe based on cationic conjugated polymer and CdTe/CdS QDs for label-free determination of glucose in human body fluids, Biosens. Bioelectron. 95 (2017) 41–47.

[27] R. Deng, X. Xie, M. Vendrell, Y.T. Chang, X. Liu, Intracellular glutathione detection using MnO(2)-nanosheet-modified upconversion nanoparticles, J. Am. Chem. Soc. 133 (2011) 20168–20171.

[28] M.D. Barnes, A. Mehta, T. Thundat, R.N. Bhargava, V. Chhabra, B. Kulkarni, On−Off blinking and multiple bright states of single europium ions in Eu3+:Y2O3 nanocrystals, J. Phys. Chem. B 104 (2000) 6099–6102.

[29] Y. Shu, J. Gao, J. Chen, J. Yan, J. Sun, D. Jin, Q. Xu, X. Hu, A near-infrared fluorescent sensor based on the architecture of low-toxic Ag2S quantum dot and MnO2 nanosheet for sensing glutathione in human serum sample, Talanta 221 (2021), 121475.

[30] M.S. Zaeimian, B. Gallian, C. Harrison, Y. Wang, J. Zhao, X. Zhu, Mn doped AZIS/ZnS nanocrystals (NCs): effects of Ag and Mn levels on NC optical properties, J. Alloys Compd. 765 (2018) 236–244.

[31] G. Huang, C. Wang, S. Xu, Z. Qi, C. Lu, Y. Cui, Ag- and Mn-doped ZnInS/ZnS dual-emission quantum dots with zone tunability in the color coordinate, Nanotechnology 27 (2016), 185602.

[32] Y. Liu, Y. Zhang, X. Zhang, W. Zhang, X. Wang, Y. Sun, P. Ma, Y. Huang, D. Song, Near-infrared fluorescent probe based on Ag&Mn:ZnInS QDs for tyrosinase activity detection and inhibitor screening, Sensor. Actuator. B Chem. 344 (2021), 130234.

[33] Y. Liu, Z. Li, S. Zou, C. Lu, Y. Xiao, H. Bai, X. Zhang, H. Mu, X. Zhang, J. Duan, Hyaluronic acid-coated ZIF-8 for the treatment of pneumonia caused by methicillin-resistant Staphylococcus aureus, Int. J. Biol. Macromol. 155 (2020) 103–109.

[34] P. Yang, G. Zhou, Phase transfer of hydrophobic QDs for water-soluble and biocompatible nature through silanization, Mater. Res. Bull. 46 (2011) 2367–2372.

[35] G. Huang, C. Wang, X. Xu, Y. Cui, An optical ratiometric temperature sensor based on dopant-dependent thermal equilibrium in dual-emitting Ag&Mn:ZnInS quantum dots, RSC Adv. 6 (2016) 58113–58117.

[36] Q. Sun, H. Bi, Z. Wang, C. Li, X. Wang, J. Xu, H. Zhu, R. Zhao, F. He, S. Gai, P. Yang, Hyaluronic acid-targeted and pH-responsive drug delivery system based on metal-organic frameworks for efficient antitumor therapy, Biomaterials 223 (2019), 119473.

[37] S. Chu, S. Wang, Y. Du, F. Yang, L. Yang, C. Jiang, Portable smartphone platform integrated with a nanoprobe-based fluorescent paper strip: visual monitoring of glutathione in human serum for health prognosis, ACS Sustain. Chem. Eng. 8 (2020) 8175–8183.

[38] Y. Cao, J. Liu, L. Zou, B. Ye, G. Li, Ratiometric fluorescence sensing of glutathione by using the oxidase-mimicking activity of MnO2 nanosheet, Anal. Chim. Acta 1145 (2021) 46–51.

[39] T. Schnelldorfer, S. Gansauge, F. Gansauge, S. Schlosser, H.G. Beger, A.K. Nussler, Glutathione depletion causes cell growth inhibition and enhanced apoptosis in pancreatic cancer cells, Cancer 89 (2000) 1440–1447.